Journal of Materials Chemistry C

Accepted Manuscript

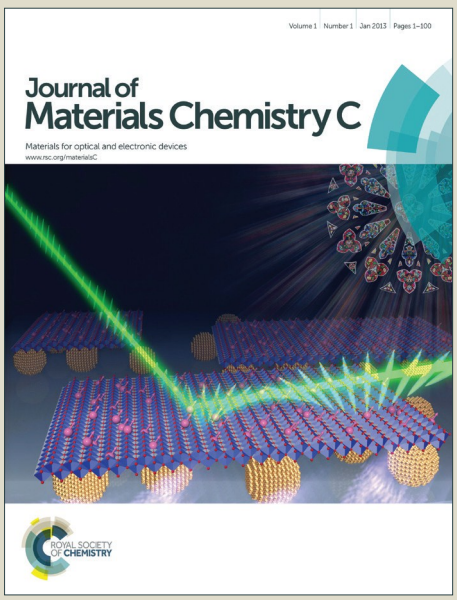

ROYAL SOCIETY OF CHEMISTRY

www.rsc.org/materialsC

Graphene-Boron Nitride Lateral Heterostructure – A First-Principles Study of its Growth, Electronic Properties, and Chemical Topology

G.C. Loh [a,b*] and Ravindra Pandey [a*]

[a]Department of Physics, Michigan Technological University, Houghton, Michigan 49931, USA
[b]Institute of High Performance Computing, 1 Fusionopolis Way, #16-16 Connexis, Singapore 138632

(March 31, 2015)

Email:
G. C. Loh (jgloh@mtu.edu)
Ravindra Pandey (pandey@mtu.edu)

Abstract

The lateral integration of graphene and hexagonal boron nitride permits intricate design of a hybrid heterostructure in which electronic characteristics can be tuned as per requirement of a particular application. Such laterally integrated hybrid nanostructures are investigated using density functional theory to explore their growth, electronic properties, and chemical topology. The evolution of energetics, geometry, density of states, number of charges, and electric dipole moment with carbon adatoms is delineated. In the triangular C-BN heterostructures, C atoms prefer to grow from the vertices as compared to the edges of the heterostructures due to their strong anchoring. Despite a small lattice mismatch between *h*-BN and graphene, the structural stability of the heterostructure depends on the number of C adatoms (i.e. stage of growth), and growth from the *B-terminated* BN flake appears to be preferred. The Cu substrate reduces the stability of the C-BN heterostructure. The heterostructures are metallic, suggesting that charge transfer effects from the Cu substrate play a dominant role in governing the electronic properties of the heterostructures. Electron localization and quantum theory of atoms in molecules illustrate the partial ionic-covalent character of the B-N bonds, which are less covalent than C-B/C-N bonds in the heterostructures. All in all, this study of the evolution of the C-BN heterostructures' characteristics with growth is a vital step towards developing hybrid nanoelectronic circuitry with precisely controlled properties.

Keywords: *h*-BN, graphene, heterostructure, growth

1. Introduction

Downscaling of modern integrated circuitry components to nanometric dimensions necessitates greater spatial precision in control over the electrical properties of electronic materials. This is especially true with the complexity in the structure of the device components, and with the range of device materials. In recent years, the 'wonder material' graphene has been explored intensively due to its ultrahigh room-temperature carrier mobility [1-4], and is touted to be the next-generation electronic material to replace silicon, since the latter is approaching its performance limits. Successful efforts have been made to induce a small bandgap of milli-eVs in the semi-metal graphene [5,6]. On the other hand, hexagonal boron nitride (*h*-BN), another two-dimensional honeycombed material, has garnered widespread interest, partially due to its graphene-like geometrical structure, with a wide bandgap of approximately 6 eV [7], which makes it an outstanding dielectric material. Furthermore, *h*-BN has superior chemical and thermal stability [8-11]. The distinct disparity in the electronic properties of graphene and *h*-BN spurred the idea of integrating them in electronic devices, in one way or another, such that the bandgap can be moderated or tuned [12-14] at selective locations in the hybrid devices.

Naturally, the next question is - how should the two materials be combined? There are numerous propositions, one of which is via the doping mechanism. Domains of graphene or BN can be created by doping boron and nitrogen atoms in graphene [15], or carbon atoms in *h*-BN [16], and hence generating a matrix of graphene and BN 'patches'. Apart from this, both materials can also be put together in its entirety of form. For example, graphene and *h*-BN can be grown or stacked on top of each other in various arrangements to form composite sheets (if they are of similar sizes) or vertical heterostructures [5,17-21] (if their sizes are dissimilar), which essentially renders them as three-dimensional nanostructures. On the other hand, assimilation can also be done laterally. These in-plane heterostructures of graphene and *h*-BN have first been synthesized by lithographical regrowth, either by regrowth of *h-BN* from the edges of patterned graphene by low-pressure chemical vapour deposition (LPCVD) [22], or the converse [23], facilitated by the highly similar lattice structure of both

materials (lattice mismatch ≈ 1.6%). In this paper, we refer Material A to be the material from which regrowth takes place, and the other material to be Material B. The crystalline quality of the hybrid heterostructure is contingent on that of the edges of Material A, which in turn is affected by factors characterizing the growth process, namely: (1) chamber pressure, (2) chamber temperature, and (3) feedstock gas partial pressure. In general, the quality of the nanostructure is reliant on the resolution of the lithography mask, and inconsistencies and imperfection of the technique are apt to create edge defects. In the context of lithographical regrowth, interfacial disorder between the two materials is prevalent. To circumvent this problem, the simplest and most direct way is to do without the lithography mask. Instead of LPCVD, atmospheric pressure chemical vapor deposition (APCVD) is used for the continuous growth of Material B from the edges of Material A [24]. To further justify the advantages of APCVD over LPCVD, irregular dendritic edges have been found in graphene by the former method [25], while the latter aids the alignment of the atoms at the edges of hexagonal graphene flakes [26-30].

Interestingly, the results of growth studies show subtle disagreements over the nature of the predominant factor controlling the lattice orientation of Material B. Ref **24** suggests that lateral templated growth can be promoted by using near-identical growth conditions for both materials. Ref **31** presenting the heteroepitaxial growth of *h*-BN from fresh graphene edges by APCVD goes further to accentuate the significance of Material A (graphene), and the substrate is relatively inconsequential to the growth of Material B (*h*-BN) [31]. The growth of the *h*-BN heteroepitaxial crystal from the one-dimensional edge of the graphene seed crystal depends only on the lattice structure of graphene, and not on the underlying copper substrate. However, if the graphene seed crystal is absent, *h*-BN aligns itself with the copper substrate. Essentially the greater importance of the 'lateral' template (edges of Material A) in inducing lattice coherence of the two materials, with respect to the 'vertical' template (substrate), was postulated in the growth studies.

In spite of such experimental studies, there is still a substantial lack of information regarding the energetics of the in-plane graphene-BN heterostructures. Which sites do the carbon atoms prefer in the initial phase of growth, when the interface between both materials is in the process of formation? How does the lattice mismatch between the two materials, albeit how small it is, affect the structural stability of these lateral heterostructures? How does the binding energy of the heterostructures change as carbon atoms become sequentially bonded to *h*-BN? What effects does a substrate such as Cu have on the electronic properties of the heterostructures? *These are relevant and imperative questions that have remained unanswered at this point. We embark upon addressing these questions with the help of density functional theory.* Since the focus is on the heterostructures in their initial growth phase, they are hereafter more appropriately named as C-BN heterostructures. Apart from the above, energetics of the heterostructures and electronic properties such as the projected density of states (PDOS), and Bader charges are calculated. Last but not least, we analyze the electron density distribution by the electron localization function (ELF) [32-34] and the quantum theory of atoms in molecules (QTAIM) [35-39], and describe the character of the chemical topology in the C-BN heterostructures.

2. Computational Model

A triangular BN flake (BN) deposited on a Cu(111) substrate is considered for electronic structure calculations. The (111) surface of the Cu substrate has been chosen since its lattice mismatch with BN is small at ~ 2%. Note that synthesis of a triangular form of the BN flake has been reported [40,41]. In fact, triangular flakes of other two-dimensional materials such as graphene [42] and molybdenum disulphide (MoS_2) [43] have also been synthesized. The substrate Cu(111) is made up of three ABC-stacked layers, and arranged in the face centered cubic (FCC) structure. It is first simulated by a (4 × 4) supercell to investigate the initial stage of growth process of C-BN heterostructure. At a later stage of the growth process with full coverage of the *h*-BN edges with C, we consider a (6 × 6) supercell for final calculations. For initial calculations, the choice of a smaller (4 × 4) cell allows us to use our

computational resources in an efficient way. Note that the flake in the (4 × 4) configuration is approximately 0.6 nm in length on each side of the triangle, and is comparable to that of the smallest quantum dots (≈ 0.8 – 1.0 nm) that have been synthesized [44-47]. Therefore the trends and qualitative conclusions are relevant and useful to get an insight into the nucleation and structure of the material.

For the triangular BN flake/Cu(111), the initial configurations considered for calculations are (1) *B-terminated; (B, N)=(top, fcc)*, (2) *N-terminated; (B, N)=(top, fcc)*, (3) *B-terminated; (B, N)=(fcc, top)*, (4) *N-terminated; (B, N)=(fcc, top)*. 'Top' and 'fcc' are the adsorption sites of the substrate, and the B and N atoms are positioned in such a way that they are either on top of or at the fcc site of the substrate (Figure 1). In the equilibrium configurations, B and N atoms in (2) and (3) occupy approximate commensurate positions on top of the substrate, while in (1) and (4), the atoms relax to incommensurate positions. To eliminate the effects of incommensurability, only (2) and (3) are considered for further calculations. Note that our choice of configurations is guided by the fact that the growth of the C-BN heterostructure is likely to be dependent on the binding strength of C to the BN flake deposited on the Cu (111) substrate.

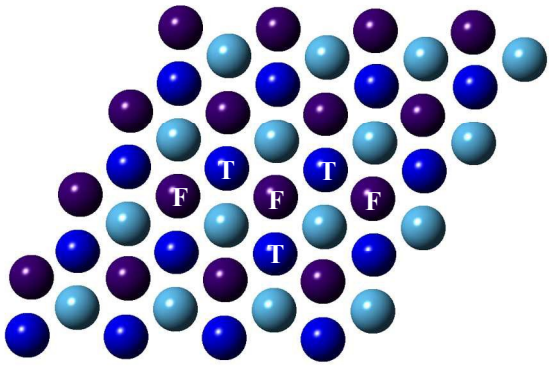

Figure 1. Top view of Cu(111) substrate, and possible adsorption sites (In purple: fcc/F; In dark blue: top/T) on the surface.

Calculations based on density functional theory (DFT) were performed with the VASP (Vienna Ab Initio Simulation Package) package, with the implementation of projector augmented-wave (PAW)

pseudopotentials [48] (with an energy cutoff of 400 eV) and the Perdew-Burke-Ernzerhof (PBE) exchange-correlation functional in the generalized gradient approximation (GGA) [49]. Dispersion correction was included in the calculations by the DFT-D2 approach of Grimme [50]. The Brillouin zone was sampled with a (9×9×1) k-point mesh using the Monkhorst-Pack scheme [51]. The structures were optimized until the forces (as calculated by the Hellmann-Feynman formalism [52,53]) were less than 10^{-5} eV/Å. In the supercell, the structure is separated from its periodic image in the direction perpendicular to the surface by a vacuum region of 12 Å. Dipole corrections were applied in the direction perpendicular to the material surface to avoid interactions between periodically repeated images.

To partition the continuous charge density among the atoms in the system, Bader's atoms in molecules theory [35-39] is implemented, such that the atomic basin is determined at the zero flux surface around the atom. This surface is observed in the two-dimensional sense at which the charge density is at a minimum perpendicular to the system surface. Therefore the total electronic charge of each atom can be defined, and the charge among the atoms distributed.

As a prior step to depositing the flake on the substrate, the geometry of the substrate is optimized. Subsequently, the BN flake is added. In calculations of the BN flake/Cu(111) structure, the geometry of the substrate is constrained, while the BN flake is fully relaxed.

3. Initial Growth Pathways

The growth of the C-BN heterostructure is extrapolated such that every B or N atom at the perimeter of the BN flake is bonded with a C atom, essentially forming a complete C-BN lateral heterostructure. Figure 2 shows the initial steps taken to simulate the growth process of C-BN heterostructure. The relative total energies of the heterostructures with different bonding sites of C are given. For the BN flake, we define the vertices to be at the points of the triangle, while an edge is

considered between two vertices. Note that *[N-terminated; (B, N)=(top, fcc)]* and *[B-terminated; (B, N)=(fcc, top)]* configurations have zigzag edges that are constituted of the same type of element at the vertices and edges. Therefore the *[N-terminated; (B, N)=(top, fcc)]* flake is made up of 6 nitrogen atoms (3 at the vertices, and 3 at the edges), and 3 boron atoms. *[B-terminated; (B, N)=(fcc, top)]* flake consists of 6 boron atoms (3 at the vertices, and 3 at the edges), and 3 nitrogen atoms. The side-view of the optimized structure of the triangular BN/Cu(111) systems is presented in Figures 3(a)(b)(e)(f) and 4(a)(b)(e)(f). The heterostructure relaxes to anchor itself with its vertex atoms nearer the Cu substrate relative to other atoms.

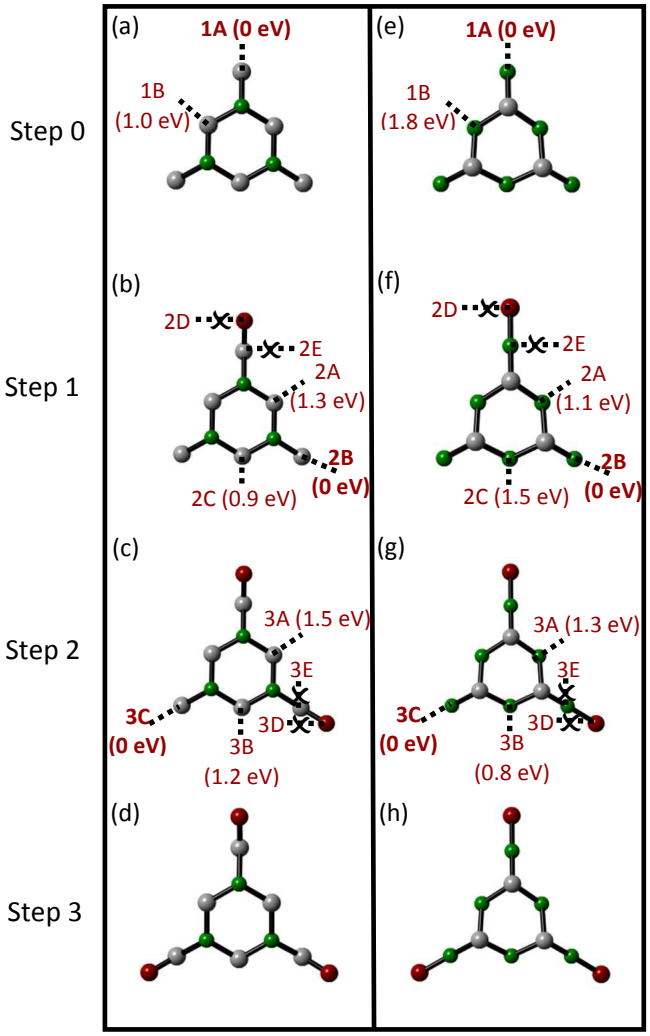

Figure 2. Growth pathways of (a)-(d) [N-terminated; (B, N)=(top, fcc)] and (e)-(h) [B-terminated; (B, N)=(fcc, top)] lateral heterostructures. The labels and dashed lines denote the bonding sites that are considered in the study. The cross symbols mark the sites at which C cannot be bound to the heterostructure, while the labels in bold refer to the sites that are most energetically favorable. The bracketed numerals refer to the relative total energies of the C-BN heterostructures, with different bonding sites of C. Atoms in green are B, grey are N, and brown are C.

Due to symmetry, some of the bonding sites of the flake are identical to those in Figure 2, and hence are redundant in this study. For example, Site 1B is only one of the three edge sites in Figures 2(a) and (b). The energetically most favorable sites are shown in bold in Steps 0 – 2, while bonds are marked with a 'cross' symbol if the C atom relaxes to occupy a position far from the initial site. The growth of C atoms from the lateral heterostructure is such that C bonding takes place at the vertices in preference over the edges. This is primarily due to the particular arrangement of the atoms in the structure. In both heterostructures, the vertex and edge atoms, which are of the same element, occupy the *fcc* sites above the Cu(111) substrate, whereas atoms of the other element are at the *top* sites. However, a C atom bonded to the edge atom is at a *top* site, while it is at an *hcp* site if it is bonded to the vertex atom. Consequently a C atom bonded at the vertex site lies in the vicinity of three neighbouring Cu atoms and forms bonds with them. The charge transfer plot of the *[N-terminated; (B, N)=(top, fcc)]* (hereafter named as *N-terminated*) system indirectly demonstrates the formation of bonds between the C atom and the three Cu atoms (Figure 3b, and more clearly in the inset; the plot is calculated by subtracting the charge density distribution of entire system by that of the substrate and the heterostructure). The accumulation regions are depicted in red, while the depletion regions are in yellow. The Cu atoms that are transferring charges with the B/N atoms are numbered. For the *[B-terminated; (B, N)=(fcc, top)]* (hereafter named as *B-terminated*) system, using the same isosurface values of 0.008 e/Å^3 (as in Figure 3b), Figure 4b shows a greater spatial distribution of charge transfer when the BN-C flake is bonded to the Cu substrate. When the C atom is bonded to the edge atom of the BN flake (Figure 3e and 4e), the transfer of charges only takes place between

the C atom and one Cu atom. This contributes largely to the more energetically favorable sites at 1A, 2B, and 3C shown in Figure 2.

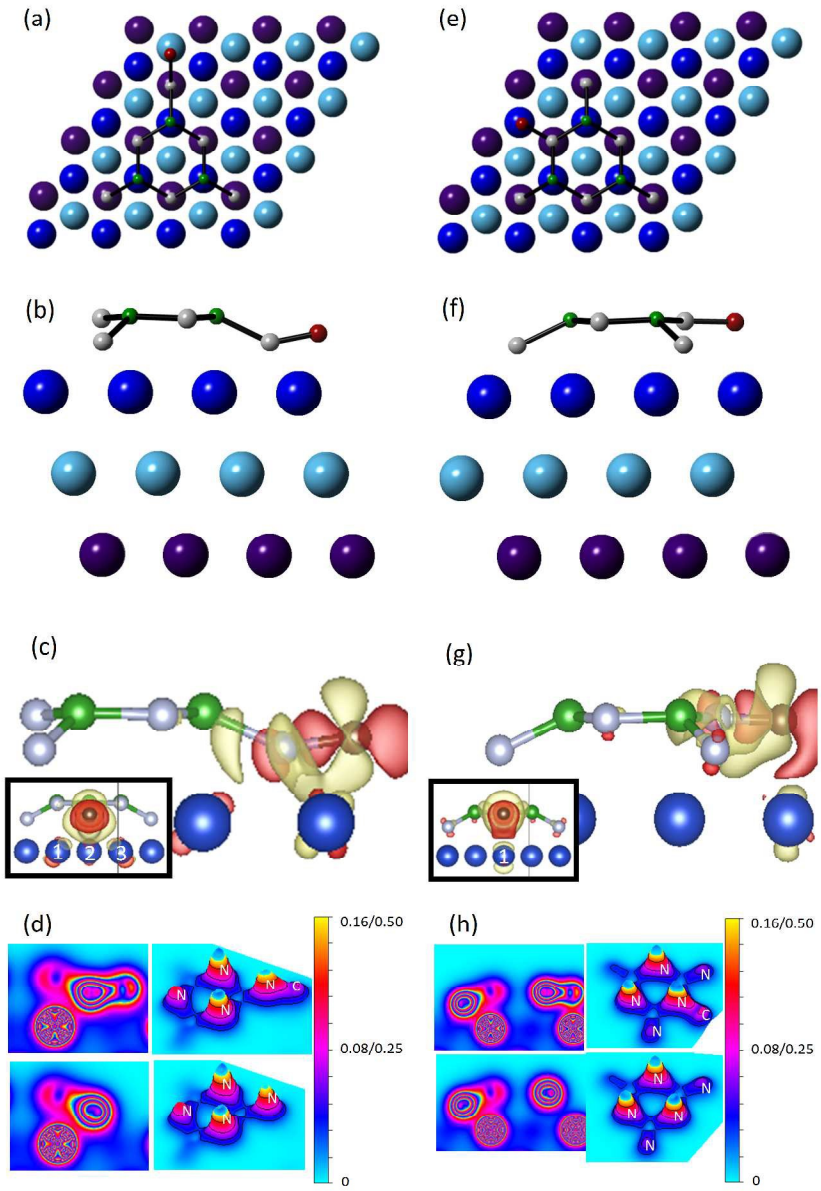

Figure 3. [N-terminated; (B, N)=(top, fcc)] lateral heterostructure. (a)(e) Top-view, (b)(f) side-view, (c)(g) charge transfer plot, (inset shows a magnified view of the interface region around the C atom; the plot is calculated by subtracting the charge density distribution of entire system by that of the substrate and the heterostructure), (d)(h) charge density landscape (top row shows the landscape with the C atom; bottom row shows the landscape without the C atom | left figures are taken through one of the central axes of the heterostructure and through the C atom; right figures are bird's eye views of the horizontal slice through the C atom). For (a)-(d), the C atom is bonded to the vertex; for (e)-(h), it is bonded to the edge. Atoms in green are B, grey are N, and brown are C. The colors dark blue, light blue, and purple are used to represent the top, middle, and bottom layers of Cu, respectively.

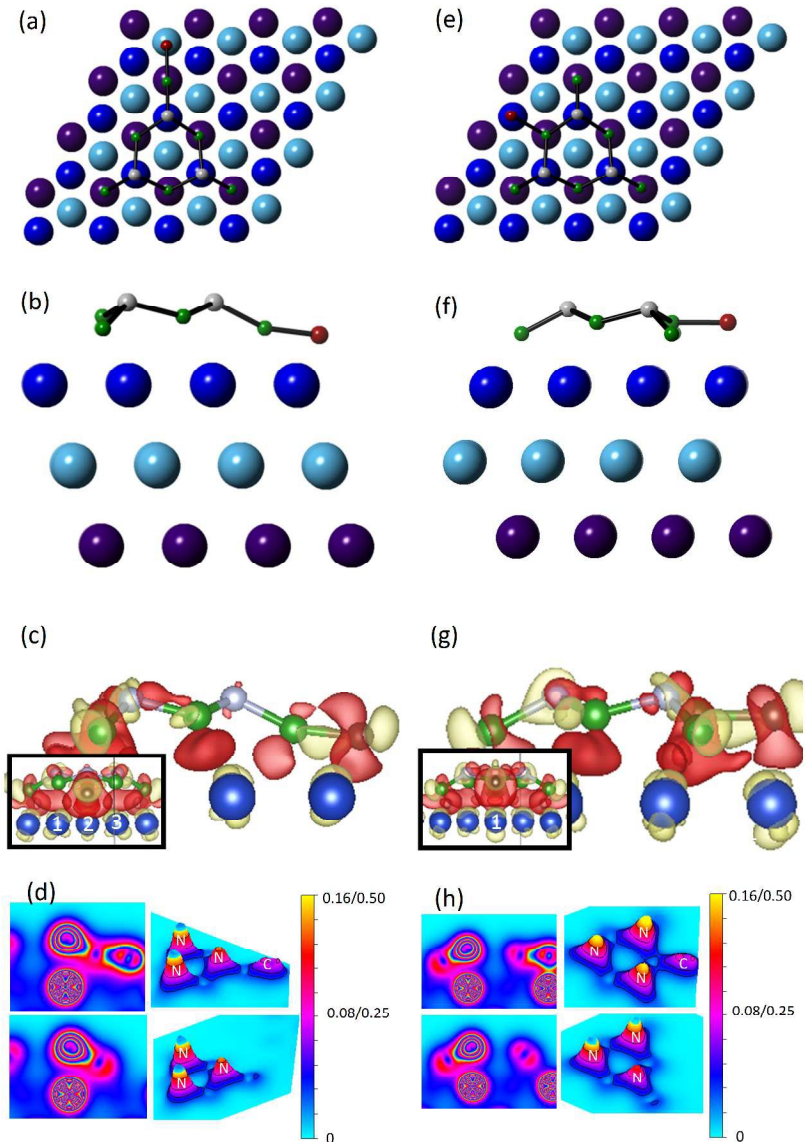

Figure 4. [B-terminated; (B, N)=(fcc, top)] lateral heterostructure. (a)(e) Top-view, (b)(f) side-view, (c)(g) charge transfer plot, (inset shows a magnified view of the interface region around the C atom; the plot is calculated by subtracting the charge density distribution of entire system by that of the substrate and the heterostructure), (d)(h) charge density landscape (top row shows the landscape with the C atom; bottom row shows the landscape without the C atom | left figures are taken through one of the central axes of the heterostructure and through the C atom; right figures are bird's eye views of the horizontal slice through the C atom). For (a)-(d), the C atom is bonded to the vertex; for (e)-(h), it is bonded to the edge. Atoms in green are B, grey are N, and brown are C. The colors dark blue, light blue, and purple are used to represent the top, middle, and bottom layers of Cu, respectively.

The charge density distribution at other regions of the heterostructure is not affected by the formation of the C-B/N bond (Figure 3(c), 3(f), 4(c), and 4(f)). Moreover, the three-dimensional bird's eye view shows that the charge density at the nitrogen atoms is largest, followed by that at carbon, and then at boron. Furthermore, there is no apparent difference in the charge density at a vertex N atom and one at an edge. The addition of a C atom does not significantly change the charge density in the B and N atoms. As the C-BN heterostructure is not planar, taking a horizontal slice inevitably excludes information that does not fall within that slice. In the vertical slice of the landscape, colours are assigned recursively to data points with values smaller or larger than the saturation levels defined.

However, the aforementioned provides only a visual approach. By using Bader's method to draw the atomic boundaries [35-39], the mean charge of the atoms in the BN/C-BN heterostructure is then more accurately probed. Contrasting the on-site charges in the heterostructure (deposited on the Cu substrate) and the triangular BN flake (without C atoms bonded to it), the change in the charges in the BN flake is then calculated, which describes the charge transfer effect induced by both the C

atoms (if any) and the Cu substrate (Figure 5). [Only the charges in the B and N atoms are included in this analysis to permit a direct comparison of the charges between the various structures. *Note* that the change in charges in Figure 5(b)-(d), (f)-(h) is with respect to the BN flake (without C atoms) in vacuum.] In the *N-terminated* system (Figure 5(a)), all atoms gain charges. The N atoms gain more charges than the B atoms. However in the *B-terminated* system (Figure 5(e)), the N atoms lose charges, while the B atoms gain charges. Since the electronegativity of N is (3.04 on Pauling scale [54]) larger than that of B (2.04), the loss of charges of N is attributed to the substrate effect.

From an inspection of the charges in the B and N atoms between growth steps, we can derive the contribution of the charge transfer effect that originates from the bonding of C atoms to the BN flake. The change in number of charges in the nearest neighboring atom to the C atom when the C atom is added to the flake is approximately 0.30 e for B and N atoms in the *N-terminated* system, whereas it is around 0.80 e in the *B-terminated* one. By summing up all the values in Figure 5 in each individual step and configuration, and finding the difference between steps, we can then quantify the effective charge transfer effect induced by the bonding of C atoms: the *N-terminated* system gains 0.40 e in the 1st step, and 0.31, and 0.49 e in the following steps. In comparison, the *B-terminated* system loses 0.90 e in the 1st step, and then 0.88, and 0.87 e in the subsequent steps. Evidently, *the C atoms have a larger charge transfer effect on the B-terminated system.*

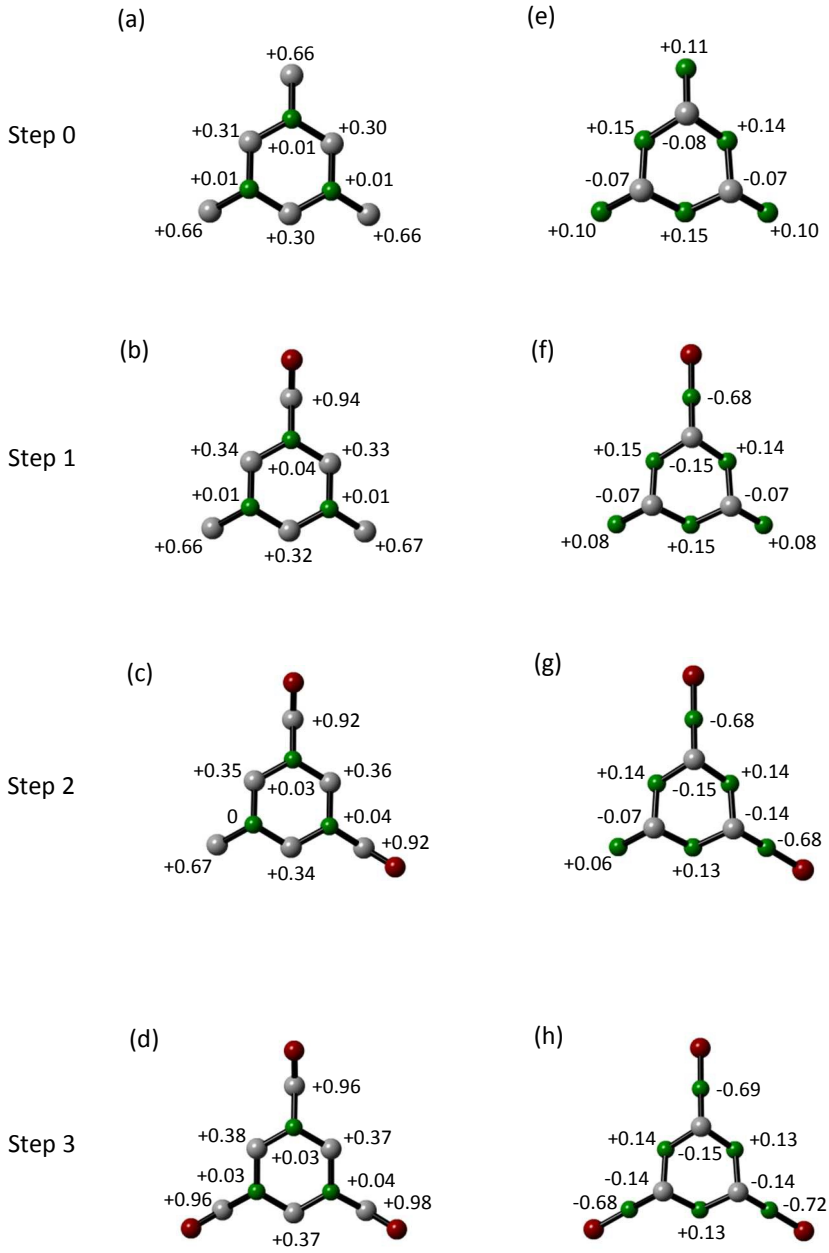

Figure 5. On-site charges in B and N atoms at each step of growth. (a)-(d): [N-terminated; (B, N)=(top, fcc)] lateral heterostructure; (e)-(h): [B-terminated; (B, N)=(fcc, top)] lateral heterostructure. Atoms in green are B, grey are N, and brown are C.

4. Evolution of Energetics, Geometrical Structure, Electronic Interaction, and Electric Dipole Moment

A complete C-BN lateral heterostructure is shown in Figure 6. The evolution of the formation energy, edge excess energy, binding energy of the heterostructure to the Cu substrate, C-N/C-B bond length, flake-substrate distance, mean charge transfer in the heterostructure (as presented in Figure 5), and electric dipole moment with the growth of the heterostructure are tabulated in Tables 1 and 2. The formation energy is defined as the difference between the total energy of the system and the sum of the energy of its constituents,

$$E_f = E_{C-BNf/Cu} - \sum_{\alpha=Cu,B,N,C} n_\alpha \mu_\alpha \quad (1)$$

where $E_{C-BNf/Cu}$ is the total energy of the BN flake-Cu substrate system, n_α is the number of atoms of a particular element α, and μ_α is the chemical potential of that element α. The formation energy quantifies the stability of a molecule, and according to Eq. 1, a more stable molecule has a more negative E_f. Both types of C-BN heterostructure become more stable with its growth, either in the presence of the Cu substrate (numeral without brackets) or in its absence (bracketed numerals). The substrate reduces the stability (i.e. smaller formation energy) of the heterostructure. The binding energy of the flake is expressed as

$$\Delta E = E_{BNf/Cu} - E_{Cu} - E_{BNf} \quad (2)$$

where $E_{BNf/Cu}$, E_{Cu}, and E_{BNf} are the total energies of the structure with the flake, without the flake, and of the flake itself. Thus, a bound flake will be associated with a negative binding energy

(Eq. 2). To check whether the supercell is sufficiently large to eliminate interaction between periodically repeated images in the x- and y- directions, we have repeated the calculation of the binding energy of the bare *[N-terminated; (B, N)=(top, fcc)]* heterostructure on a (6 × 6) Cu(111) substrate (Supporting Information: Figure S1). The binding energy is calculated to be -1.696 eV/atom, which is less than 0.5% from that on a (4 × 4) Cu(111) substrate (to 3 decimal places: -1.700 eV/atom). In the initial growth phase with 1 to 3 C atoms, the binding energy of the *N-terminated* heterostructure decreases with an increase in number of C atoms. This is in stark contrast to that of the *B-terminated* heterostructure in which the binding energy increases. However for both configurations, the binding energy in the complete C/BN form is lower than that in their initial growth phase. The formation energy and binding energy of the complete *N-terminated* heterostructure is lower than that of the *B-terminated* one. In other words, the *N-terminated* heterostructure is less stable, and this agrees exactly with **Ref. 24** which shows that there is transfer of charges from N to C, resulting in the occupation of antibonding states to form weaker interfaces.

Nevertheless, both heterostructures differ not only in the way C is bonded to the BN flake, i.e. C-N bonds in the *N-terminated* flake, and C-B in the *B-terminated* one, but also the sites at which the atoms are positioned on the Cu substrate. Essentially, the dissimilitude in how the characteristics of the heterostructures evolve with growth (Tables 1 and 2) reflects both the substrate effect ('vertical' template) and the edge-termination effect ('lateral' template).

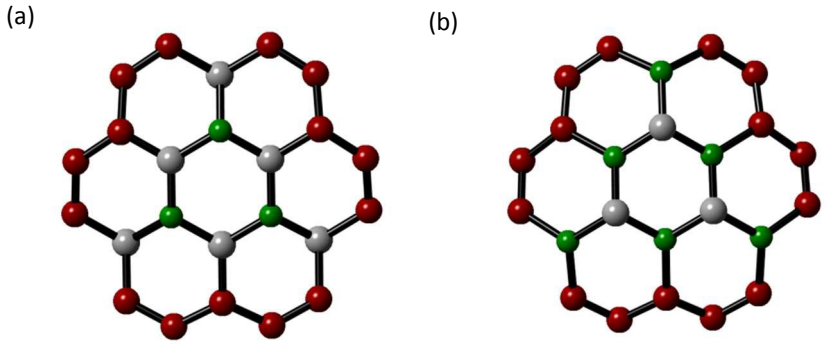

Figure 6. Top views of complete C-BN lateral heterostructure in the (a) [N-terminated; (B, N)=(top, fcc)], and (b) [B-terminated; (B, N)=(fcc, top)] configuration. Atoms in green are B, grey are N, and brown are C.

Table 1. [N-terminated; (B, N)=(top, fcc)] heterostructure deposited on Cu(111) substrate: Energetics, structural, and electronic properties. The formation energy and bond length of the heterostructure in the absence of the Cu substrate are shown in brackets.

Adatoms	+0C	+1C	+2C	+3C	Complete
Energetics					
Formation Energy (eV/atom)	-3.65 (-3.96)	-4.31 (-5.25)	-4.85 (-5.45)	-5.28 (-5.67)	-5.85 (-6.10)
Edge Excess Energy/Length (nN)	3.77	3.14	2.62	2.21	4.88
Binding Energy (eV/atom)	-1.70	-1.17	-0.69	-0.30	-0.09
Structure					
C-N Bond Length (Å)	-	1.28 (1.19)	1.28 (1.19)	1.27 (1.19)	1.52 (1.19)
Flake-Substrate Distance (Å)	1.74	1.72	1.70	1.70	1.67
Electronic Interaction					
Total Charge Transfer (e/atom)	0.32	0.37	0.40	0.46	0.50
Electrostatic					
Electric Dipole Moment (eV/Å)	-0.37	-0.36	-0.30	-0.21	-0.42

Table 2. [B-terminated; (B, N)=(fcc, top)] heterostructure deposited on Cu(111) substrate: Energetics, structural, and electronic properties. The formation energy and bond length of the heterostructure in the absence of the Cu substrate are shown in brackets.

Adatoms	+0C	+1C	+2C	+3C	Complete
Energetics					
Formation Energy (eV/atom)	-4.32 (-4.78)	-4.33 (-4.79)	-4.36 (-4.86)	-4.39 (-5.21)	-6.28 (-6.49)
Edge Excess Energy/Length (nN)	1.21	0.90	0.58	0.27	3.31
Binding Energy (eV/atom)	-1.25	-1.38	-1.42	-1.43	-0.48
Structure					
C-B Bond Length (Å)	-	1.47 (1.44)	1.45 (1.60)	1.44 (1.66)	1.56 (1.52)
Flake-Substrate Distance (Å)	1.80	1.75	1.71	1.68	1.97
Electronic Interaction					
Total Charge Transfer (e/atom)	0.06	-0.04	-0.14	-0.24	-0.28
Electrostatic					
Electric Dipole Moment (eV/Å)	-0.30	-0.26	-0.20	-0.12	-0.01

We define the edge excess energy as the difference between the sum of the bond energies in the heterostructure and the sum of the bond energies in the dimer configuration [55],

$$\gamma = \frac{1}{L}\left[\sum_{\beta=B-N,C-N,C-B} n_\beta\left(E_{\beta,bond} - E_{\beta,dim}\right)\right] \quad (3)$$

where n_β is the number of bonds between two atoms denoted by β, $E_{\beta,bond}$ is the mean bond energy in the heterostructure, $E_{\beta,dim}$ is the bond energy in the dimer configuration, and L is the length of the edge. For the heterostructure, the mean bond energy ($E_{\beta,bond}$) is the difference in total energies of the heterostructure and its constituents divided by the number of bonds in the heterostructure. In a particular heterostructure, the same value of $E_{\beta,bond}$ is used in the derivation of the excess energy of each edge. For the dimer, the mean bond energy ($E_{\beta,dim}$) is the difference in total

energies of the dimer (for example B-N or C-N) and its constituents. The bond energy of B-N, N-C, C-C, and B-C is calculated to be -4.63, -8.24, -7.11, and -4.12 eV, respectively. As there is a lattice mismatch (1.6%) between graphene and BN monolayers, albeit how small it is, the bonding of C atoms to the BN flakes will induce a non-trivial amount of in-plane strain in this nanoscale lateral heterostructure. For both configurations, the edge excess energy per unit length (hereby simplified as 'edge excess energy') is reduced with the initial growth (1 to 3 C atoms), but when the complete heterostructure is formed, there is a significant large increase in excess energy. In general, the *B-terminated* heterostructure has a smaller edge excess energy than the *N-terminated* one.

The change in average charge transfer during growth is listed in Tables 1 and 2. The gain (loss) in charges in the *N-terminated* (*B-terminated*) heterostructure increases with the bonding of C atoms to the BN flake. The net charge in the *B-terminated* heterostructure with 1 or 2 C atoms attached is relatively small although the binding energy is non-trivial at about -1.30 eV/atom. Likewise, although the *B-terminated* heterostructure has a larger charge transfer effect (Figure 5), the change in formation energy as it grows is generally smaller than that for its counterpart. This suggests that the charge transfer is not likely to be the dominant factor in its stability and binding strength to the substrate. However, the evolution of the electric dipole moment is reflected by the charge transfer effect; the change in electric dipole moment is greater in the *B-terminated* heterostructure, which is probably due to the stronger charge transfer effect induced by the C atoms as the C atoms are bonded to the BN flake.

Subsequently, the sensitivity of the energetics of the lateral heterostructures in response to an external electric field is studied (Tables S1 and S2). The electric field is applied in the direction perpendicular to the heterostructure surface. In general, the formation energy and edge excess energy (which is calculated from the formation energy using Eqn (3)) increase with the electric field strength in the positive direction. Notably, the change in the edge excess energy ranges from 5-10%. On the other hand, a direct relationship between variations in binding energy with the electric field is not

observed, although the change of the binding energy with the field strength approaches 10% in a few cases.

5. Density of States

The density of states (DOS) are calculated and projected onto the atomic orbitals of boron and nitrogen in the two forms of BN flake/C-BN heterostructure to characterize the atomic contributions to the energy bands (Figures 7 and 8). The heterostructures at each stage of growth are metallic, suggesting the significance of charge transfer effects from the Cu(111) substrate. The x and y directions are defined within the plane of the heterostructure, while the z direction is taken to be perpendicular to the surface of the material. Only the contribution of the p_x and p_y orbitals is presented; the p_z DOS is simply the difference between the total DOS and the sum of the p_x and p_y DOS. For B, the magnitude of the in-plane p-DOS (sum of p_x and p_y) of B is significantly larger than that of its out-of-plane p_z-DOS at the Fermi level (Figures 7 and 8). In comparison, for N, the magnitude of p_y-DOS is much smaller than that of p_x- and p_z-DOS. This is justified by the charge density plot at Γ and the Fermi level for the *B-terminated* heterostructure with 1 C atom (Figure S2). Moreover, with 1 to 3 C atoms bonded to the heterostructure, the energy bands in the N atoms are dominated by the p_x states. Most of the states in B and N atoms of both configurations occupy energy levels between E_F-10 eV to E_F (Figures 7 and 8). As more C atoms are bonded to the *N-terminated* BN flake, the B and N atoms gain more charges (Table 1), and the DOS of both species shift to lower energies (Figure 7). Similarly, the loss of more charges in the *B-terminated* BN flake with more C atoms bonded (Table 2) induces a upward shift of energies of the occupied DOS with respect to the Fermi level (Figure 8). Strong hybridization of the occupied p_x and p_y states near the Fermi level is observed in the complete *B-terminated* C-BN heterostructure, but not in its *N-terminated* counterpart.

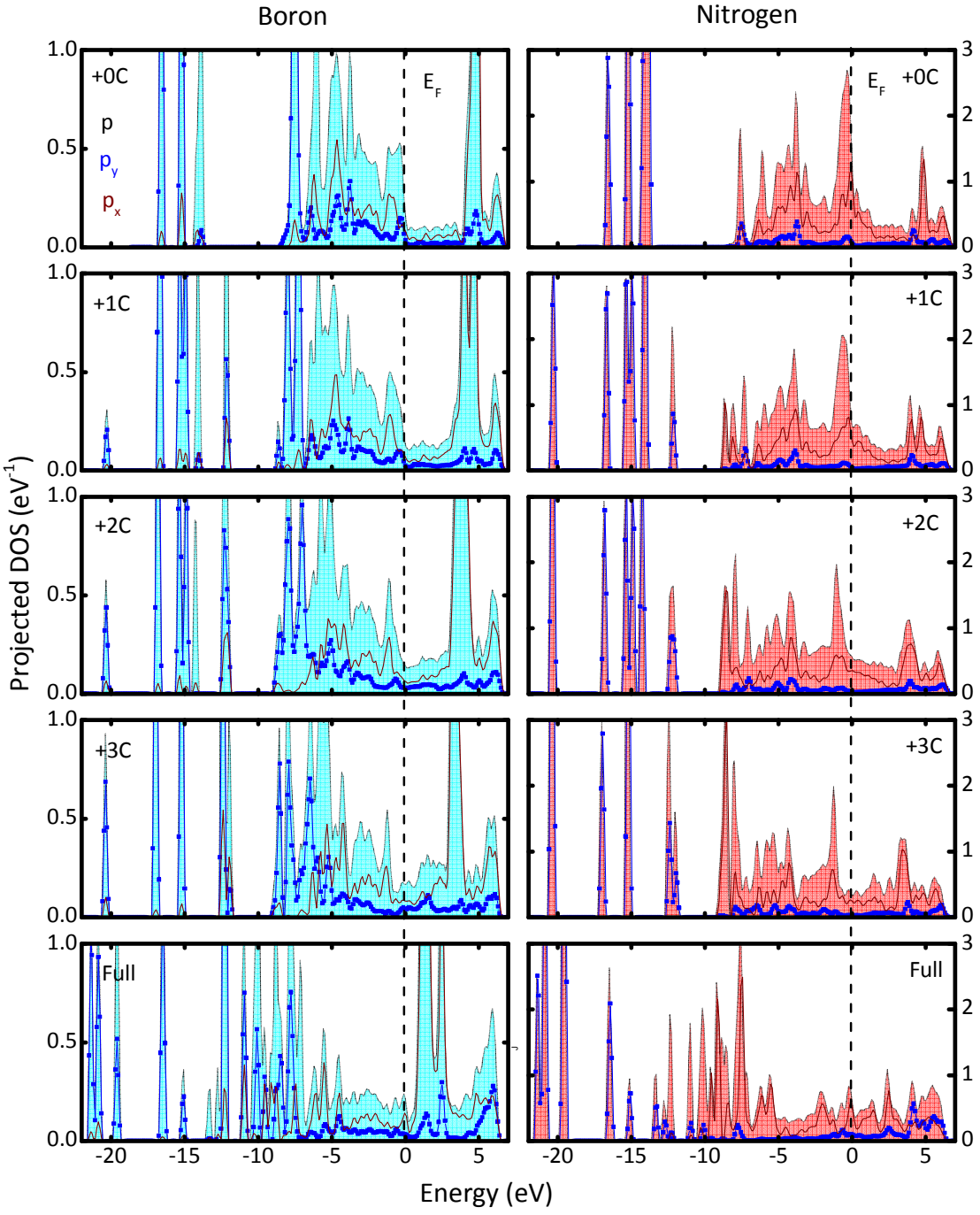

Figure 7. Atomic orbital projected density of states of [N-terminated; (B, N)=(top, fcc)] heterostructure. Zero is taken to be Fermi energy.

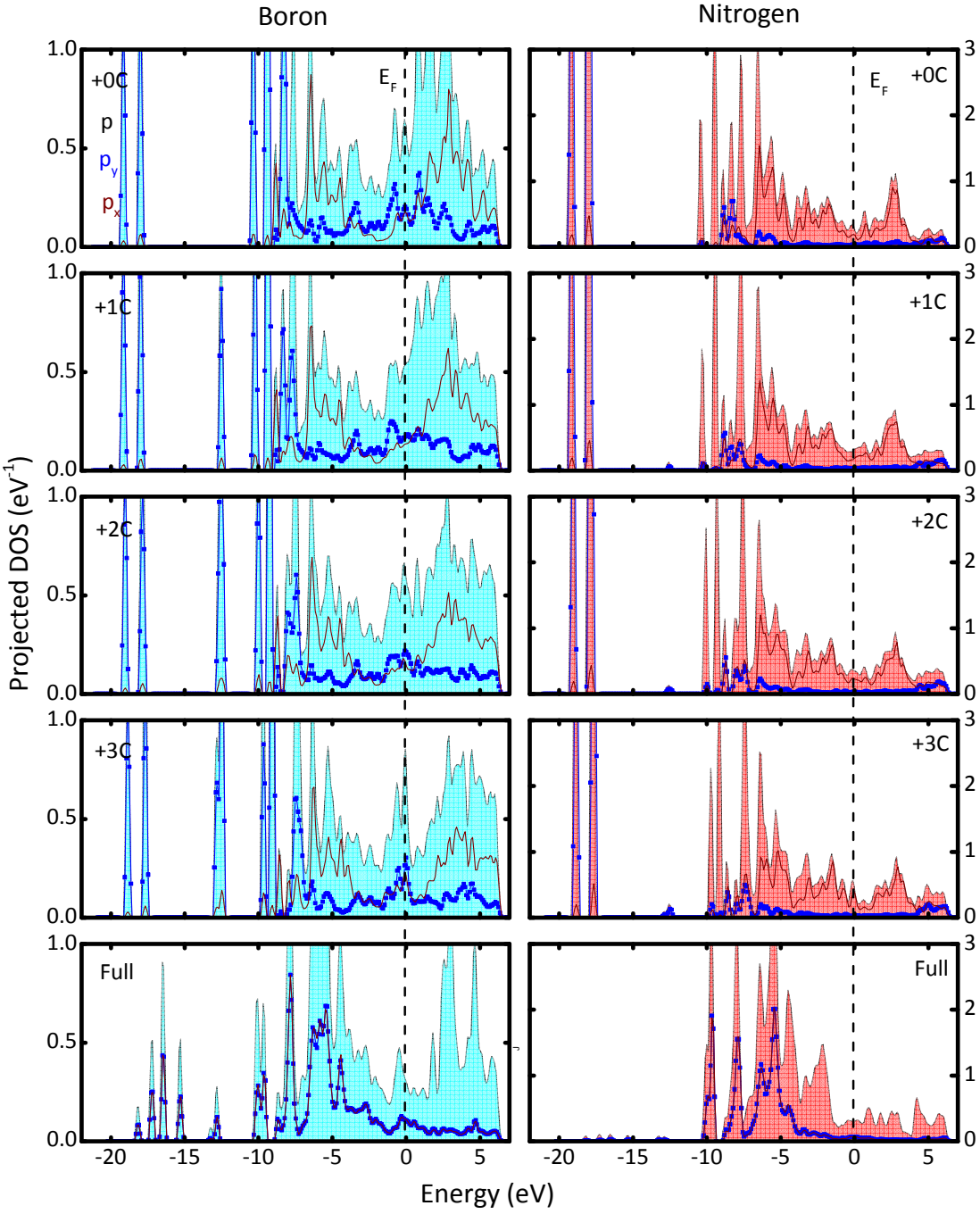

Figure 8. Atomic orbital projected density of states of [B-terminated; (B, N)=(fcc, top)] heterostructure. Zero is taken to be Fermi energy.

6. Chemical Topology

The chemical bond, or more specifically, the electron density distribution between atoms can be described accurately by two tools - the first is the electron localization function (ELF) [32-34], and the second is the Laplacian of the electron density via the quantum theory of atoms in molecules [35-39]. The ELF is a measure of the likelihood of finding an electron in the vicinity of a reference electron located at a particular point, with the same spin [56]. Mathematically

$$ELF = \left\{1 + \left[\frac{C(\vec{r})}{C_h(\rho(\vec{r}))}\right]^2\right\}^{-1} \quad (4)$$

where $\vec{r}$ is the radial distance from the nucleus, and ρ is electron spin density. It ranges from 0 to 1, with it approaching 1 when r is within the pair region, and it is small when r is close to the border between two pair regions. In a homogeneous electron gas, the ELF is 0.5 at every location. The covalency of the bond is primarily delineated by the form of the charge attractors; if they are more spherically distributed around the cores of the atoms, the interaction is more ionic or highly van der Waals in nature. In a more covalent bond, the attractor is more symmetric about the cores, while still lying on the bond line connecting the cores. The number and form of the localization regions are strongly dependent on the choice of the ELF isovalue, and conventionally, an isovalue of approximately 0.80-0.85 is used for valence compounds.

In Figures 9(a)(b), the ELF of isovalues 0.50, 0.65, and 0.82 are plotted for the *N-terminated* flake/heterostructure. The ELF for the first two isovalues serves as reference for that of isovalue 0.82. The localization region of isovalue 0.82 is slightly asymmetrical about the center point between any B-N pair (especially between the B atom and the vertex N atom in Figure 9(a) where the region envelopes a part of the N atom), with the region having a marginally larger distribution nearer the N atom (Figure 9(a)-(c)). This suggests that the B-N bond is not completely covalent – it is slightly ionic

in character. In the complete C-BN heterostructure (Figure 9(b)(c)), the electrons at a C atom with 2 neighbouring C atoms and a N atom (marked by black dotted box in Figure 9(b)) have a larger localization region between any C-C pair than between the C-N pair. Similarly, the electrons at a N atom with a neighbouring B atom and 2 C atoms (marked by red dotted box in Figure 9(b)) have a larger localization region between the B-N pair than between the C-N pair. This implies that electrons are more localized between a C-N pair than a B-N pair or a C-C pair, i.e. [C-N]>[B-N]/[C-C]. 2 two-dimensional slices of Figure 9(c) are taken, and the electron localization landscape is drawn in Figures 9(d); the asymmetry of the localization region presented in Figure 9(a)-(c) is also apparent in Figure 9(d) whereby the value of the ELF is larger around the N atom (and C atom) than around the B atom. In general, the localization region between a C-C pair is much more symmetrical than between a pair of different species.

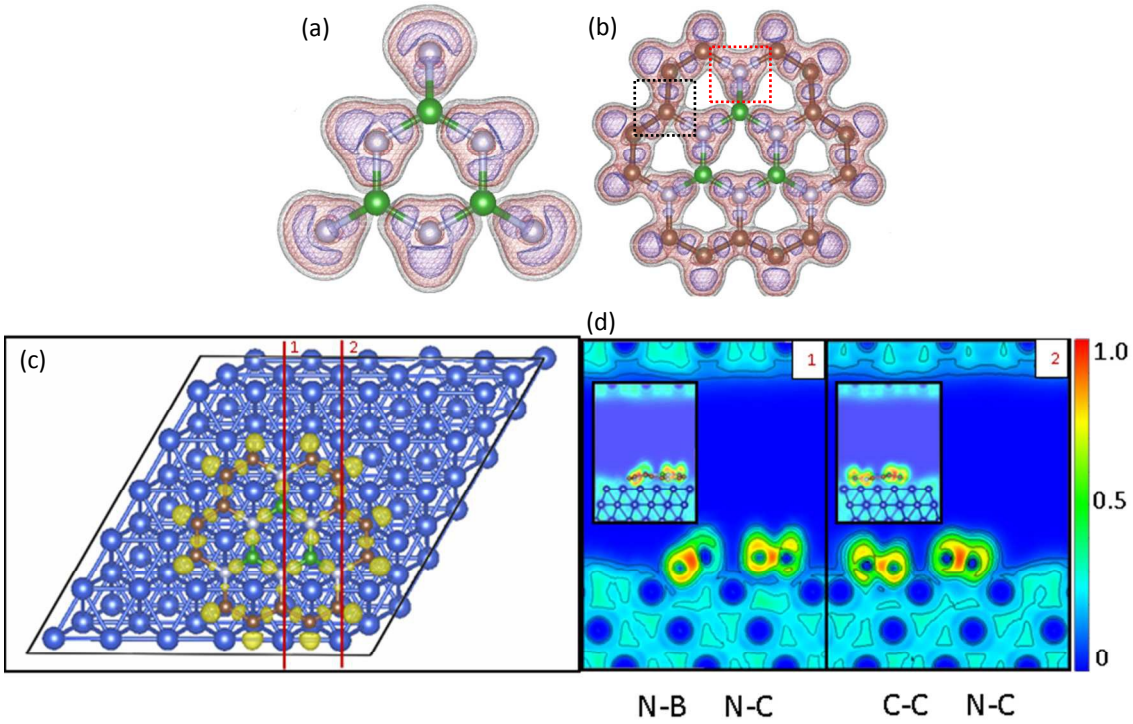

Figure 9. Electron localization landscape of [N-terminated; (B, N)=(top, fcc)] flake/heterostructure. Top views of (a) BN flake, (b) C-BN heterostructure, and (c) C-BN heterostructure with Cu substrate. The dotted boxes in (b) mark the neighbouring region around the N and C atoms, which is then described in Section 6. 2D slices along two planes in (c) are shown, and the landscape presented in (d). The insets include stick-and-ball schematics of the atoms. Atoms in green are B, grey are N, and brown are C.

Akin to the *N-terminated* flake/heterostructure, in the *B-terminated* case (Figure 10(a)-(c)), the localization region of isovalue 0.82 is asymmetrical about the center point between the B-N pairs, and skewed slightly towards the N atom. However in the complete C-BN heterostructure (Figure 10(b)(c)), the electrons at a C atom with 2 neighbouring C atoms and a B atom (marked by black dotted box in Figure 10(b)) have a larger localization domain between the C-B pair than between any C-C pair. The electrons at a B atom with a neighbouring N atom and 2 C atoms (marked by red dotted box in Figure 10(b)) have a larger localization region between the C-B pair than between the B-N pair. Therefore electron localization is relatively weaker in the C-B pair than C-C/B-N pair. The

2D electron localization landscape in the B-terminated heterostructure (Figure 10(d)) describes a similar chemical topology as that in the N-terminated case, with the value of ELF larger around the N atom (and C atom) than around the B atom.

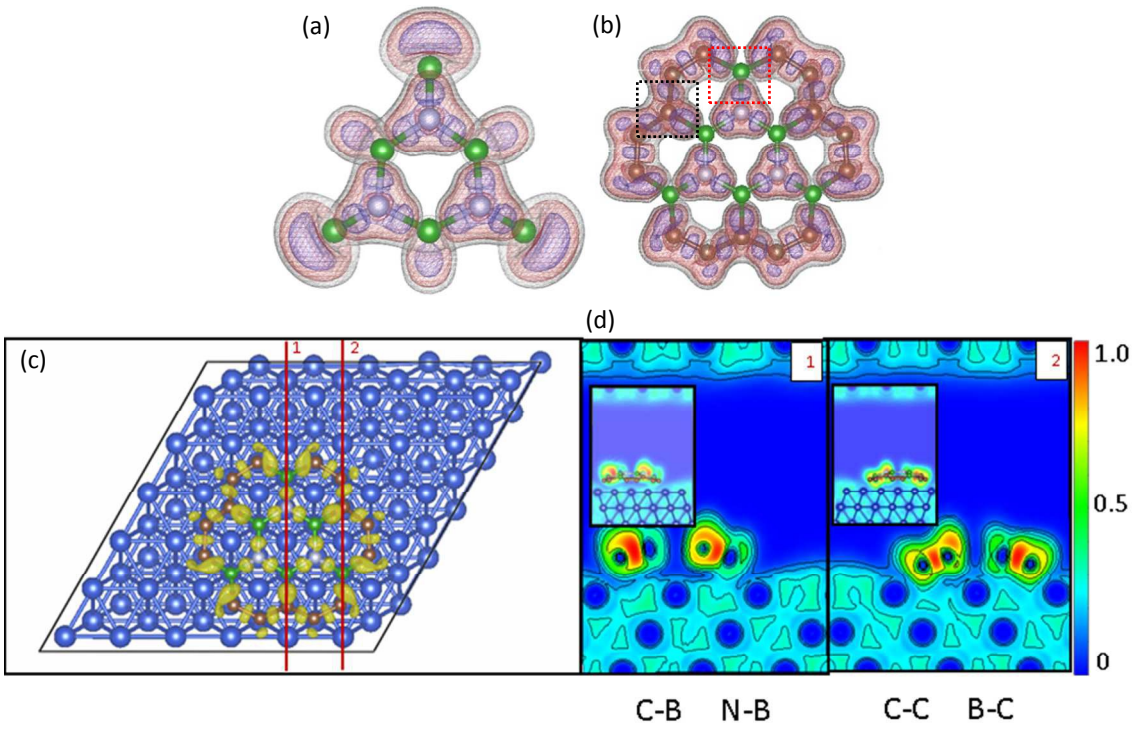

Figure 10. Electron localization landscape of [B-terminated; (B, N)=(fcc, top)] heterostructure. Top views of (a) BN flake, (b) C-BN heterostructure, and (c) C-BN heterostructure with Cu substrate. The dotted boxes in (b) mark the neighbouring region around the B and C atoms, which is then described in Section 6. 2D slices along two planes in (c) are shown, and the landscape presented in (d). The insets include stick-and-ball schematics of the atoms. Atoms in green are B, grey are N, and brown are C.

The second tool is the Laplacian of the electron density. Mathematically, the Laplacian operator is a second derivative or the trace of the Hessian of a function; it denotes the local minimum/maximum,

or in other words, the saddle point of that function. Both minimum and maximum points are *critical points* at which the first derivatives of the function become zero. In the context of chemical topology, the differential operator reproduces the spherical shell structure of isolated atoms by alternating shells of charge concentration and shells of charge depletion [39,57]. The outermost shell of charge concentration of an atom is called the valence shell charge concentration (VSCC), and its spherical symmetry is broken when the atom bonds with another atom. Another feature in the Laplacian plot of the electron density is the nuclear critical point (NCP), which is a local maximum in electron density, and is typically located at the position of a nucleus. A zero-flux surface contains a set of Laplacian trajectories which terminate at the bond critical point (bcp) where the Laplacian equals zero.

In general, the covalency of the bonds is expressed by (1) the form of the zero envelope of the negative Laplacian, and (2) the value of the negative Laplacian at the bcp. Figure 11 shows the negative Laplacian plots of the N- and B-terminated BN and C-BN flakes/heterostructures, in three-dimensional and two-dimensional view. The grey dots represent the bcp in the charge profile. There are 3 bcp in the vicinity of each B atom, suggesting that *there is interaction between the N atoms*. All bcp are surrounded by the zero envelope of the negative Laplacian - the bonds between the B and N atoms are predominantly covalent, though it has a slight ionic character (as shown in Figures 9 and 10). The BCCs, and the locally maximum and minimum densities are marked in Figure 11; the negative Laplacian values of the maxima and minima are shown in green and red respectively. The extension of the *N-terminated* BN flake to a C-BN heterostructure causes a significant drop of the local maximum Laplacian at the N atom from 86 to 64 e/Å^5, while it only reduces from 64 to 63 e/Å^5 in the case of the *B-terminated* heterostructure. This complements the observation in Tables 1 and 2 that the charge transfer induced by the C atoms in the complete C-BN heterostructure is more significant in the *N-terminated* case (0.50 e/atom versus -0.28 e/atom).

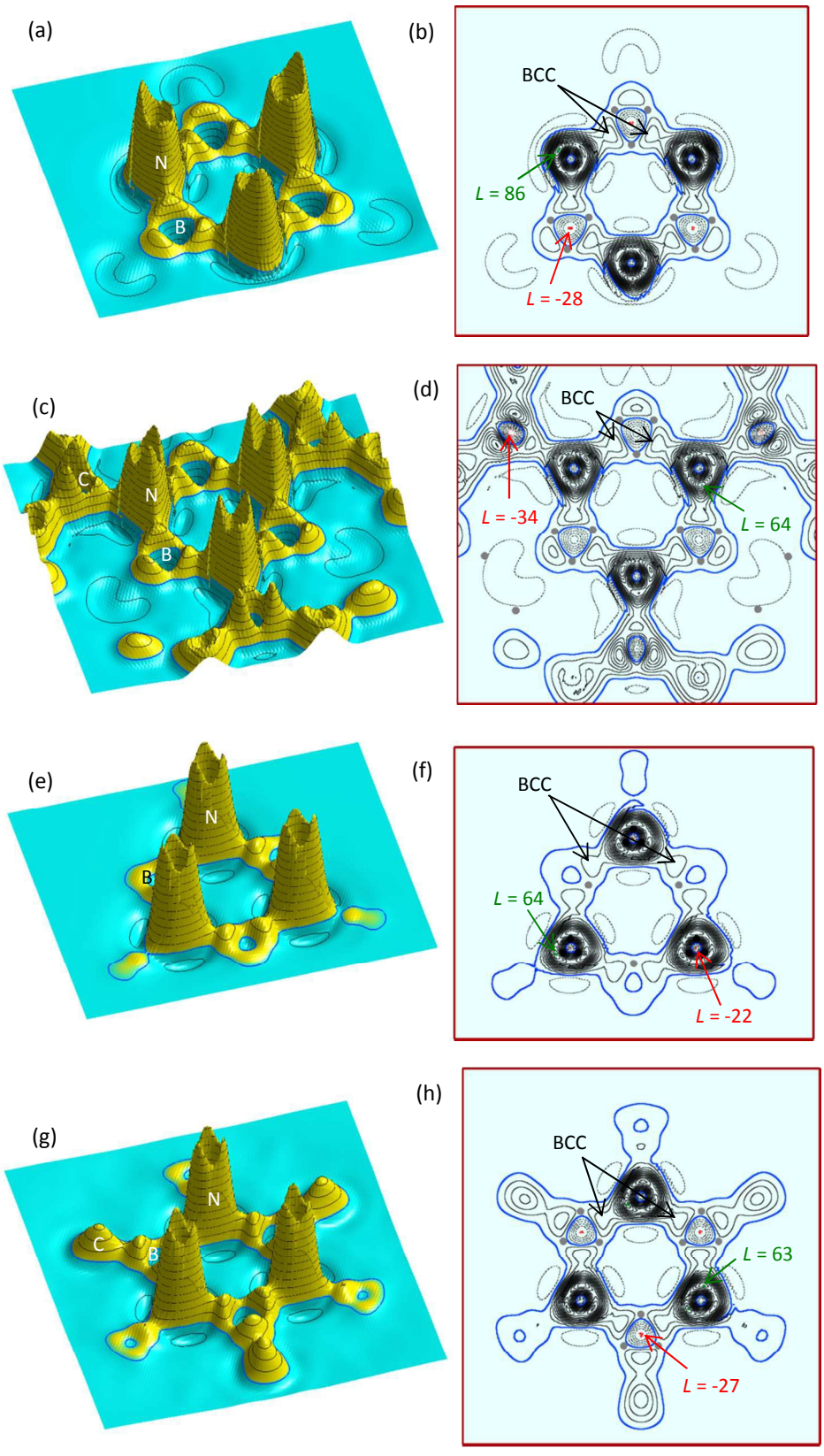

Figure 11. Negative Laplacian plots of (a)(b) [N-terminated; (B, N)=(top, fcc)] BN flake, (c)(d) [N-terminated; (B, N)=(top, fcc)] C-BN heterostructure, (e)(f) [B-terminated; (B, N)=(fcc, top)] BN flake, and (g)(h) [B-terminated; (B, N)=(fcc, top)] C-BN heterostructure. (a), (c), (e), and (g) are 3D plots, while (b), (d), (f), and (h) are 2D plots.

Figure 12 compares the kinetic energy density, potential energy density, and electronic energy density at one of the vertices of each flake/heterostructure. This particular region is selected to feature the chemical topology of the different types of bond, namely B-N and C-B/C-N bonds. The electronic energy density plots complement the negative Laplacian plots (Figure 11); it is more negative if the bond has a greater covalent character. The energy density between the B and N atoms in the flakes/heterostructures (*N*- and *B-terminated*, BN and C-BN) is dark-blue-to-blue on the colour bar, which corresponds to approximately -0.01 $E_h a_0^{-3}$, whereby E_h is hartree and a_0 is Bohr radius. Comparatively, the energy density between the C and B/N atoms is light blue (~-0.03 $E_h a_0^{-3}$). Therefore, the B-N bonds are less covalent than C-B/N bonds in all configurations, regardless of the type.

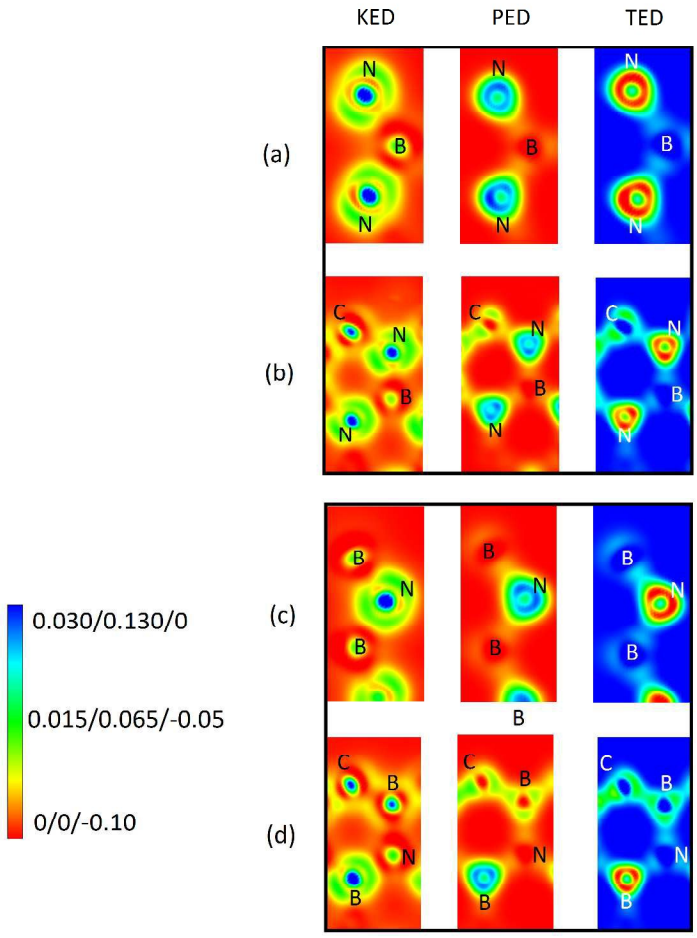

Figure 12. Kinetic energy density (KED), potential energy density (PED), and electronic energy density (TED) of (a) [N-terminated; (B, N)=(top, fcc)] BN flake, (b) [N-terminated; (B, N)=(top, fcc)] C-BN heterostructure, (c) [B-terminated; (B, N)=(fcc, top)] BN flake, and (d) [B-terminated; (B, N)=(fcc, top)] C-BN heterostructure. The colour bar shows the energy density in $E_h a_0^{-3}$*, whereby* E_h *is hartree and* a_0 *is Bohr radius.*

7. Summary

Graphene and hexagonal boron nitride have vastly divergent electronic properties. By integrating them in a controlled fashion to form complex hybrid heterostructures in electronic devices, these

properties can be tailored to suit different applications. In this study, first-principles calculations with density functional theory are performed to investigate the growth, electronic properties, and chemical topology of graphene-boron nitride lateral heterostructures. The energetics (such as formation energy, edge excess energy, binding energy), geometry (C-N/C-B bond length, flake-substrate distance), number of charges, and electric dipole moment of each system in every phase of its growth are computed and contrasted to chart their change with the growth of the heterostructure. These are summarized as follow:

(1) *Growth*: The growth of C atoms from either the *N-* or *B-terminated* triangular heterostructure is more energetically preferential at the vertices as compared to at the edges. Despite a small lattice mismatch between B/N and C, the structural stability of the heterostructure changes with its growth. The substrate reduces the stability of the heterostructure. In the initial growth phase, the binding energy of the *N-terminated* heterostructure decreases with the increase in number of C atoms. On the other hand, the converse is observed in the *B-terminated* heterostructure. However, in their complete C-BN lateral configurations, the binding energy is lower than that in its initial growth phase.

(2) *Electronic properties*: The heterostructures are metallic, likely due to charge transfer effects from the Cu(111) substrate. C atoms have a larger effect on the electronic properties of the *B-terminated* heterostructure. Strong bonds between the B and N atoms arise due to the predominantly σ states of the energy bands of B and N atoms at the Fermi level.

(3) *Chemical topology*: The strong B-N bonds have been shown to be slightly ionic in character from the electron localization landscape and analyses of negative Laplacian plots using QTAIM. Moreover, the B-N bonds are less covalent than C-B/C-N bonds in all configurations.

ACKNOWLEDGEMENTS

G. C. L. gratefully acknowledges A*STAR for funding under the A*STAR International Fellowship (2013-2015). The computations were performed on the MTU Superior cluster, and support from Dr. S. Gowtham is appreciated.

ASSOCIATED CONTENT

Supporting Information

[N-terminated; (B, N)=(top, fcc)] heterostructure on a (6 × 6) Cu(111) substrate. Charge density landscape of *[B-terminated; (B, N)=(fcc, top)]* heterostructure with 1 C atom. Variation of formation energy, edge excess energy, and binding energy with external electric field.

AUTHOR INFORMATION

Corresponding Authors

*(G. C. L.) E-mail: jgloh@mtu.edu

*(R. P.) E-mail: pandey@mtu.edu

Notes

The authors declare no competing financial interest.

REFERENCES

(1) Novoselov, K. S.; Geim, A. K.; Morozov, S. V.; Jiang, D.; Zhang, Y.; Dubonos, S.V.; Grigorieva, I. V.; Firsov, A. A. Electric field effect in atomically thin carbon films. *Science* **2004**, *306*, 666-669.

(2) Zhang, Y.; Tan, Y. –W.; Stormer, H. L.; Kim, P. Experimental observation of the quantum hall effect and Berry's phase in graphene. *Nature* **2005**, *438*, 201-204.

(3) Bolotin, K. I.; Sikes, K. J.; Jiang, Z.; Klima, M.; Fudenberg, G.; Hone, J.; Kim, P.; Stormer, H. L. Ultrahigh electron mobility in suspended graphene. *Solid State Commun.* **2008**, *146*, 351-355.

(4) Chen, J. H.; Jang, C.; Xiao, S. D.; Ishigami, M.; Fuhrer, M. S. Intrinsic and extrinsic performance limits of graphene devices on SiO_2. *Nat. Nanotechnol.* **2008**, *3*, 206-209.

(5) Quhe, R.; Zheng, J.; Luo, G. L.; Liu, Q.; Qin, R.; Zhou, J. N.; Yu, D.; Nagase, S.; Mei, W. –N.; Gao, Z. et al. Tunable and sizable band gap of single-layer graphene sandwiched between hexagonal boron nitride. *NPG Asia Mater.* **2012**, *4*, e6.

(6) Ni, Z. H.; Yu, T.; Lu Y. H.; Wang Y. Y.; Feng, Y. P.; Shen, Z. X. Uniaxial strain on graphene: Raman spectroscopy study and band-gap opening. *ACS Nano* **2008**, *2*, 2301-2305.

(7) Pakdel, A.; Zhi, C.; Bando, Y.; Golberg, D. Low-dimensional boron nitride nanomaterials. *Mater. Today* **2012**, *15*, 256-265.

(8) Golberg, D.; Bando, Y.; Kurashima, K.; Sato, T. Synthesis and characterization of ropes made of BN multiwalled nanotubes. *Scr. Mater.* **2001**, *44*, 1561-1565.

(9) Chen, Y.; Zou, J.; Campbell, S. J.; Le Caer, G. Boron nitride nanotubes: Pronounced resistance to oxidation. *Appl. Phys. Lett.* **2004**, *84*, 2430-2432.

(10) Zobelli, A.; Ewels, C. P.; Gloter, A.; Seifert, G. Vacancy migration in hexagonal boron nitride. *Phys. Rev. B* **2007**, *75*, 094104.

(11) Xu, Z.; Golberg, D.; Bando, Y. In situ TEM-STM recorded kinetics of boron nitride nanotube failure under current flow. *Nano Lett.* **2009**, *9*, 2251-2254.

(12) Zhang, A.; Teoh, H. F.; Dai, Z. H.; Feng, Y. P.; Zhang, C. Band gap engineering in graphene and hexagonal BN antidot lattices: a first principles study. *Appl. Phys. Lett.* **2011**, *98*, 023105.

(13) Fiori, G.; Betti, A.; Bruzzone, S.; Iannacone, G. Lateral graphene-*h*BCN heterostructures as a platform for fully two-dimensional transistors. *ACS Nano* **2012**, *6*, 2642-2648.

(14) Fan, X.; Shen, Z.; Liu, A. Q.; Kuo, J. –L. Band gap opening of graphene by doping small boron nitride domains. *Nanoscale* **2012**, *4*, 2157-2165.

(15) Chang, C. –K.; Kataria, S.; Kuo, C. –C.; Ganguly, A.; Wang, B. –Y.; Hwang, J. –Y.; Huang, K. –J.; Yang, W. –H.; Wang, S. –B.; Chuang, C. –H. et al. Band gap engineering of chemical vapor deposited graphene by in situ BN doping. *ACS Nano* **2013**, *7*, 1333-1341.

(16) Wei X.; Wang, M. –S.; Bando, Y.; Golberg, D. Electron-beam-induced substitutional carbon doping of boron nitride nanosheets, nanoribbons, and nanotubes. *ACS Nano* **2011**, *5*, 2916-2922.

(17) Britnell, L.; Gorbachev, R. V.; Jalil, R.; Belle, B. D.; Schedin, F.; Mishchenko, A.; Georgiou, T.; Katsnelson, M. I.; Eaves, L.; Morozov, S. V. et al. Field-effect tunneling transistor based on vertical graphene heterostructures. *Science* **2012**, *335*, 947-950.

(18) Dean, C. R.; Young, A. F.; Meric, I.; Lee, C.; Wang, L.; Sorgenfrei, S.; Watanabe, K.; Taniguchi, T.; Kim, P.; Shepard, K. L. et al. Boron nitride substrates for high-quality graphene electronics. *Nat. Nanotechnol.* **2010**, *5*, 722-726.

(19) Zhong, X.; Yap, Y. K.; Pandey, R.; Karna, S. P. First-principles study of strain-induced modulation of energy gaps of graphene/BN and BN bilayers. *Phys. Rev. B* **2011**, *83*, 193403.

(20) Zhong, X.; Amorim, R. G.; Scheicher, R. H.; Pandey, R.; Karna, S. P. Electronic structure and quantum transport properties of trilayers formed from graphene and boron nitride. *Nanoscale* **2012**, *4*, 5490-5498.

(21) Wu, M. M.; Zhong, X.; Wang, Q.; Sun, Q.; Pandey, R.; Jena, P. Anisotropy and transport properties of tubular C-BN Janus nanostructures. *J. Phys. Chem. C* **2011**, *115*, 23978-23983.

(22) Levendorf, M. P.; Kim, C. –J.; Brown, L.; Huang, P. Y.; Havener, R. W.; Muller, D. A.; Park, J. Graphene and boron nitride lateral heterostructures for atomically thin circuitry. *Nature* **2012**, *488*, 627-632.

(23) Liu, Z.; Ma, L.; Shi G.; Zhou, W.; Gong, Y.; Lei, S.; Yang, X.; Zhang, J.; Yu, J.; Hackenberg, K. P. et al. In-plane heterostructures of graphene and hexagonal boron nitride with controlled domain sizes. *Nat. Nanotechnol.* **2013**, *8*, 119-124.

(24) Han, G. H.; Rodríguez-Manzo, J. A.; Lee, C. –W.; Kybert, N. J.; Lerner, M. B.; Qi, Z. J.; Dattoli, E. N.; Rappe, A. M.; Drndic, M.; Charlie Johnson, A. T. Continuous growth of hexagonal graphene and boron nitride in-plane heterostructures by atmospheric pressure chemical vapor deposition. *ACS Nano* **2013**, *7*, 10129-10138.

(25) Li, X.; Magnuson, C. W.; Venugopal, A.; Tromp, R. M.; Hannon, J. B.; Vogel, E. M.; Colombo, L.; Ruoff, R. S. Large-area graphene single crystals grown by low-pressure chemical vapor deposition of methane on copper. *J. Am. Chem. Soc.* **2011**, *133*, 2816-2819.

(26) Luo, Z.; Kim, S.; Kawamoto, N.; Rappe, A. M.; Johnson, A. T. C. Growth of hexagonal shape graphene flakes with zigzag edges. *ACS Nano* **2011**, *11*, 9154-9160.

(27) Vlassiouk, I.; Regmi, M.; Fulvio, P.; Dai, S.; Datskos, P.; Eres, G.; Smirnov, S. Role of hydrogen in chemical vapor deposition growth of large single-crystal graphene. *ACS Nano* **2011**, *5*, 6069-6076.

(28) Wu, B.; Geng, D.; Guo, Y.; Huang, L. M.; Xue, Y.; Zheng, J.; Chen, J.; Liu, Y.; Jiang, L.; Hu, W. Equiangular hexagon-shape-controlled synthesis of graphene on copper surface. *Adv. Mater.* **2011**, *23*, 3522-3525.

(29) Yu, Q.; Jauregui, L. A.; Wu, W.; Colby, R.; Tian, J.; Su, Z.; Cao, H.; Liu, Z.; Pandey, D.; Wei, D. et al. Control and characterization of individual grains and grain boundaries in graphene grown by chemical vapor deposition. *Nat. Mater.* **2011**, *10*, 443-449.

(30) Gao, L.; Ren, W.; Xu, H.; Jin, L.; Wang, Z.; Ma, T.; Ma, L. –P.; Zhang, Z. T.; Fu, Q.; Peng, L. –M. et al. Repeated growth and bubbling transfer of graphene with millimeter-size single crystal grains using platinum. *Nat. Commun.* **2012**, *3*, 1-7.

(31) Liu, L.; Park, J.; Siegel, D. A.; McCarty, K. F.; Clark, K. W.; Deng, W.; Basile, L.; Idrobo, J. C.; Li, A. –P.; Gu, G. Heteroepitaxial growth of two-dimensional hexagonal boron nitride template by graphene edges. *Science* **2014**, *343*, 163-167.

(32) Savin, A.; Nesper, R.; Wengert, S.; Fässler, T. F. ELF: The electron localization function. *Angew. Chem. Int. Ed. Engl.* **1997**, *36*, 1808-1832.

(33) Poater, J.; Duran, M.; Solà, M.; Silvi, B. Theoretical evaluation of electron delocalization in aromatic molecules by means of atoms in molecules (AIM) and electron localization function (ELF) topological approaches. *Chem. Rev.* **2005**, *105*, 3911-3947.

(34) Alikhani, M. E.; Fuster, F.; Silvi, B. What can tell the topological analysis of ELF on hydrogen bonding. *Structural Chem.* **2005**, *16*, 203-210.

(35) Bader, R. F. W. *Atoms in molecules. A quantum theory*; Clarendon Press: Oxford, 1994.

(36) Bader, R. F. W. Atoms in molecules. *Acc. Chem. Res.* **1985**, *18*, 9-15.

(37) Bader, R. F. W. A quantum theory of molecular structure and its applications. *Chem. Rev.* **1991**, *91*, 893-928.

(38) Sagar, R. P.; Ku, A. C. T.; Smith, V. H. Jr.; Simas, A. M. The Laplacian of the charge density and its relationship to the shell structure of atoms and ions. *J. Chem. Phys.* **1988**, *88*, 4367.

(39) Shi, Z.; Boyd, R. J. The shell structure of atoms and the Laplacian of the charge density. *J. Chem. Phys.* **1988**, *88*, 4375.

(40) Kim, K. K.; Hsu, A.; Jia, X.; Kim, S. M.; Shi, Y.; Hofmann, M.; Nezich, D.; Rodriguez-Nieva, J. F.; Dresselhaus, M.; Palacios, T. et al. Synthesis of monolayer hexagonal boron nitride on Cu foil using chemical vapour deposition. *Nano Lett.* **2012**, *12*, 161-166.

(41) Guo, N.; Wei, J.; Fan, L.; Jia, Y.; Liang, D.; Zhu, H.; Wang, K.; Wu, D. Controllable growth of triangular hexagonal boron nitride domains on copper foils by an improved low-pressure chemical vapour deposition method. *Nanotechnology* **2012**, *23*, 415605.

(42) Lu, J.; Yeo, P. S. E.; Gan, C. K.; Wu, P.; Loh, K. P. Transforming C_{60} molecules into graphene quantum dots. *Nat. Nanotechnol.* **2011**, *6*, 247-252.

(43) Najmaei, S.; Liu, Z.; Zhou, W.; Zou, X.; Shi, G.; Lei, S.; Yakobson, B. I.; Idrobo, J. –C.; Ajayan, P. M.; Lou, J. Vapour phase growth and grain boundary structure of molybdenum disulphide atomic layers. *Nat. Mater.* **2013**, *12*, 754-759.

(44) Zhang, R.; Emge, T. J.; Zheng, C.; Li, J. The first single-sized (~1 nm) and periodically ordered array of In_2Te_3 semiconductor quantum dots self-assembled in solution. *J. Mater. Chem. A*, **2013**, *1*, 199.

(45) Baruah, U.; Gogoi, N.; Konwar, A.; Deka, M. J.; Chowdhury, D.; Majumdar, G. Carbon dot based sensing of dopamine and ascorbic acid. *J. Nanoparticles*, **2014**, *2014*, 178518.

(46) Barreiro, A.; van der Zant, H. S. J.; Vandersypen, L. M. K. Quantum dots at room temperature carved out from few-layer graphene. *Nano Lett.* **2012**, *12*, 6096-6100.

(47) Tyagi, C. Sharma, A.; Kurchania, R. Synthesis of CdS quantum dots using wet chemical co-precipitation method. *J. Non-Oxide Glasses* **2014**, *6*, 23-26.

(48) Kresse, G.; Joubert, D. From ultrasoft pseudopotentials to the projector augmented-wave method. *Phys. Rev. B* **1999**, *59*, 1758.

(49) Perdew, J. P.; Burke, K.; Ernzerhof, M. Generalized gradient approximation made simple. *Phys. Rev. Lett.* **1996**, *77*, 3865.

(50) Grimme, S. Semiempirical GGA-type density functional constructed with a long-range dispersion correction. *J. Comput. Chem.* **2006**, *27*, 1787-1799.

(51) Monkhorst, H. J.; Pack, J. D. Special points for Brillouin-zone integrations. *Phys. Rev. B* **1976**, *13*, 5188.

(52) Hellmann, H. *Einführung in die quantenchemie*; Leipzig, 1937.

(53) Feynman, R. P. Forces in molecules. *Phys. Rev.* **1939**, *56*, 340.

(54) Pauling, L. Atomic radii and interatomic distances in metals. *J. Am. Chem. Soc.* **1947**, *69*, 542-553.

(55) Lu, Q.; Huang, R. Excess energy and deformation along free edges of graphene nanoribbons. *Phys. Rev. B* **2010**, *81*, 155410.

(56) Becke, A. D.; Edgecombe, K. E. A simple measure of electron localization in atomic and molecular systems. *J. Chem. Phys.* **1990**, *92*, 5397.

(57) Sagar, R. P.; Ku, A. C. T.; Smith, V. H. Jr.; Simas, A. M. The Laplacian of the charge density and its relationship to the shell structure of atoms and ions. *J. Chem. Phys.* **1988**, *88*, 4367-4374.